Optics and Lasers in Engineering 160 (2023) 107276

Contents lists available at ScienceDirect

Optics and Lasers in Engineering

journal homepage: www.elsevier.com/locate/optlaseng

Quantitative microbolometer-based thermoelastic stress analysis

Irene Jiménez-Fortunato [a,*], Daniel J. Bull [a], Ole T. Thomsen [b], Janice M. Dulieu-Barton [b]

[a] School of Engineering, University of Southampton, United Kingdom
[b] Bristol Composites Institute, University of Bristol, United Kingdom

ARTICLE INFO

Keywords:
Infrared cameras
Thermoelastic stress analysis
Microbolometers

ABSTRACT

The use of microbolometers for Thermoelastic Stress Analysis (TSA) has the potential of substantially reducing deployment costs, as well as providing more compact and lightweight solutions in comparison to more costly, bulky and less rugged photon detector based infrared cameras. However, microbolometer performance in terms of response time and sensitivity is less than what can be achieved with photon detectors. As the use of microbolometers for TSA is becoming more widespread, it is timely to devise a means of assessing microbolometer performance and identifying the limitations of using such a system for TSA. A simulation approach is devised that enables the effect of the microbolometer response time on transient signals (such as that from TSA) to be investigated. As the TSA involves measuring a small transient temperature change, usually induced by sinusoidal cyclic loading, the simulation approach also includes the effect of a noisy non-sinusoidal signal. To identify any deleterious effects cause by a cyclic load, the transient temperature change is also generated using an optical chopper and a black body source. The variables studied are the Signal-to-Noise Ratio (SNR), the impact of different waveforms, variation in the signal mean, as well as in-built system features such as the noise reduction. A new experimentally validated calibration approach is presented that accounts for the microbolometer response time and rolling averages introduced by inbuilt noise reduction features. It is shown the calibration approach is independent of specimen material and camera frame rates, and it is demonstrated on a CFRP test specimen containing a hidden crack.

1. Introduction

Thermoelastic Stress Analysis (TSA) [1] is a well-known non-contact full-field imaging technique that has been used extensively on a variety of materials and structural components over the past three decades [2–6]. TSA depends on the thermoelastic effect, which is based on the relationship between thermal energy and mechanical deformation under elastic loading [1]. Usually, a sinusoidal cyclic load is applied to the test component to generate the small thermoelastic temperature change, ΔT, which, under adiabatic conditions is related to the sum of the principal stresses and for isotropic materials [1] is as follows:

$$\Delta T = -T_0 K \Delta(\sigma_1 + \sigma_2) \tag{1}$$

where T_0 is the mean temperature of the cycle, $\Delta\sigma_1$ and $\Delta\sigma_2$ are the change in the principal stresses, and K is the thermoelastic response defined as:

$$K = \frac{\alpha}{\rho C_p} \tag{2}$$

where ρ is the density, C_p is the specific heat capacity at constant pressure, and α is the coefficient of linear thermal expansion.

ΔT is also known as the thermoelastic response or signal, and is obtained using an infrared (IR) camera that records the temperature on the surface of the sample during the test. The IR cameras commonly used for TSA contain a photon detector sensor [7]. These have a practically instantaneous response to changes in temperature, of the order of microseconds (10 – 20,000 μs [8]), enabling accurate detection of the transient thermoelastic temperature change resulting from the cyclic loading. However, photon detectors are bulky, heavy, and expensive (~£100k), and have limited life-span due to the fatigue loading on the sensor assembly from the temperature cycling resulting from the cryogenic cooling. Therefore, significant interest has developed in using cost-effective microbolometer IR cameras for TSA, as they typically cost an order of magnitude less than photon detectors, are more lightweight and compact, and are more robust as they do not require a cooling system.

Rajic and his co-workers, e.g. [9–11] have pioneered the use of microbolometers in TSA. A detailed account of the applicability of developing microbolometer based TSA was provided in [10], where the technique was applied on an aircraft structural component. The work demonstrated the capability of microbolometers and pointed to possible future directions. Whilst microbolometer cameras have significant benefits over photon detector cameras, their major drawback, particu-

* Corresponding author at: School of Enginerring, University of Southampton, United Kingdom.
E-mail address: ijf1a17@soton.ac.uk (I. Jiménez-Fortunato).

https://doi.org/10.1016/j.optlaseng.2022.107276
Received 23 March 2022; Received in revised form 23 August 2022; Accepted 9 September 2022
Available online 30 September 2022

larly in the context of TSA, is that they have response times of the order of milliseconds that is intrinsic to the detector construction. Typically, time constants range from 7 ms to 15 ms [9, 12]. In [11], the important limiting feature of the relatively long detector response time was discussed, and a calibration approach proposed to account for the filtering effect on the measurement of transient temperatures. In contrast, in [13] and [14] the digital level (DL) output from the camera was used and the 'known stress calibration' procedure presented in [15] was applied. The stress calibration approach is not ideal as it is dependant on the IR detector responsivity and specimen surface temperature, in addition to the material properties of the test specimen. Moreover, when using microbolometers for TSA, the approach used in [14] and [15] is also highly dependant on the loading frequency. The reason for this is that as loading frequency increases, the rate of change of temperature increases, and the effect of the detector response time becomes more prominent. In [11], the calibration approach presented was independent of loading frequency, but was time consuming, as it required the use of an optical chopper and a blackbody, and must be carried out pixel by pixel on each frame of the temperature field captured by the IR camera.

In the present paper, a new procedure for calibration applicable for TSA using microbolometers is presented. The procedure preserves the practical simplicity of that described in [14] but is independent of loading frequency. It is dependant on the detector construction, but accounts for the effect of the response time on thermal measurements after TSA processing and requires no additional equipment. Hence, data processing time is significantly reduced and a practical means of applying TSA in a quantitative manner with low cost and compact microbolometers is demonstrated. The work described in the present paper will pave the way for application of TSA to large scale structures as acquisition and operational costs are significantly reduced enabling deployment of multiple low-cost microbolometer cameras and permanent installation for structural health monitoring.

To put the work in context, the paper starts with a brief overview of the working principles of microbolometers, which includes an evaluation of the FLIR A655sc [16] used in the experimental work described in the paper. Of particular importance is the thermal time constant, so an independent verification of the manufacturer's quoted value is carried out using an optical chopper and a flat plate black body. This is followed by a brief overview of the theory associated with TSA and a description of the image processing algorithms used to extract the thermoelastic response from a thermal image series. A Simulink model is presented that aids in understanding how the quality of the input signal from the microbolometer image series affects the derived thermoelastic response. The model is used to perform a detailed study on the effects of inaccuracy in loading frequency, and drift in the mean levels of temperature and noise. A key feature of microbolometer systems are in-built noise reduction (NR) features that make use of the temporal richness of the image data; the effect of the NR feature on the thermoelastic response is also studied. A parametric experimental verification that confirms the findings from the model is presented, examining the effect of frame rate, loading amplitude and frequency, material and the NR feature. Finally, a new approach to calibrating the thermoelastic response is described and applied to a carbon fibre reinforced polymer (CFRP) sample with an internal defect, the results of which are validated by comparing the TSA from the microbolometer images to those obtained from a photon detector.

2. Microbolometer operation and experimental validation

2.1. Microbolometer working principle

Microbolometers are formed of an array of sensing elements that are continuously exposed to radiation. Each element has an IR radiation absorbing layer (metal or semiconductor) that changes its resistance depending on the amount of absorbed energy. The change in resistance is converted into a voltage that is transformed to a digital signal in units of digital level (DL). The signal in DL is converted into temperature by means of a radiometric calibration that is dependant only on the temperature, as the thermal time constant is fixed and determined by the sensor material. Hence, in contrast to a photon detector the response time of a microbolometer is not instantaneous [7, 12], but it is expressed as follows:

$$\frac{ouput(t)}{output(t \rightarrow \infty)} = 1 - e^{-\frac{t}{\tau_{th}}} \tag{3}$$

where t is time and τ_{th} is the thermal time constant.

In TSA, it is necessary to apply a cyclic loading to the test specimen and hence the temperature, T, changes at a rate determined by the loading frequency. To account for the thermal time constant, the magnitude of the temperature response, $|T(\omega)|$, and phase, $\angle T(\omega)$, [7, 11] are expressed as follows:

$$|T(\omega)| = \frac{C}{\sqrt{1 + \omega^2 \tau_{th}^2}} \tag{4}$$

$$\angle T(\omega) = \tan^{-1}\left(-\tau_{th}\omega\right) \tag{5}$$

where C is a constant that is dependant on the sensor construction and ω is the loading frequency in rad/s.

As the microbolometer is constantly exposed to radiation, the electrical resistance of the sensor also changes constantly according to the rate of the transient signal. Typically, a microbolometer requires usually three times the thermal time constant to obtain 95% of the final signal magnitude, and six times the thermal time constant to achieve 99% [12], so the sensor does not have time to stabilise. If the sensor has not reached the correct temperature, it outputs the current temperature at that time. Hence, the temperature value is attenuated in the manner of a low-pass filter [7, 11] as indicated by Eqs. (4) and (5). Therefore, when using a microbolometer for measurement from an object with a cyclic temperature change, as with TSA, a reduction in the magnitude of the temperature change is recorded as well as a shift in phase depending on the loading frequency.

Low-pass filters have a cut-off frequency [17], $f_{cut-off}$, which in the case of TSA is the loading frequency where the output falls below 70.7% of the input, and is defined as:

$$f_{cut-off} = \frac{1}{2\pi\tau_{th}} \tag{6}$$

The microbolometer frame rate (number of frames that can be captured per second) provides the temporal richness of the measurements but is limited by the row-by-row readout from the sensor. It causes a delay between the top left pixel and the bottom right pixel of the image as shown in [18] and represents a major drawback for microbolometer cameras. For this reason, the frame rates that can be selected are divisions of the maximum frame rate. For example, for the microbolometer FLIR A655sc used in this work (Table 1), the maximum readout time

Table 1
Characteristics of FLIR A655sc [16].

Detector material	VOx
Spectral Range	7.5 - 14 μm
Cost	~£10,000
Maximum frame rate at full window	50 Hz
Frame rate selection at full window	50 Hz, 25 Hz, 12.5 Hz, 6.25 Hz, 3.13 Hz
Reading array	Each row of pixel detectors at a time
Thermal time constant	< 8 ms - fixed
Cut-off frequency	19.9 Hz
Response time	24 ms (3 x thermal time constant)
Sensitivity (NETD)	< 30 mK
Resolution	640 x 480 pixels
Cooling	No
Weight	0.9 kg
Size	216 x 73 x 75 mm

is 41.6 μs per row at full frame, considering that there are 480 rows of pixels, the maximum frame rate at full frame is 50 Hz. Hence, the frame rates that can be selected at full frame are 50 Hz, 25 Hz, 12.5 Hz, 6.25 Hz and 3.12 Hz. In contrast, the readout from a photon detector is sensor-by-sensor providing faster frame rates. Therefore, microbolometers require longer sample times to reduce the noise content, considering the sensors generally have higher Noise Equivalent Temperature Difference (NETD). To circumvent this, microbolometers are often fitted with NR features that exploit the temporal richness of the data, by taking a rolling average over several frames of data. This is acceptable when the signal is stationary but for transient signals introduces a further filtering effect. However, the setup is much faster as there is no cool-down period required compared to the photon detectors [10]. Also, the Noise Equivalent Temperature Difference (NETD) of microbolometers is usually higher than photon detectors, but the post-processing algorithms, such as lock-in and least-squares, applied to the temperature data will filter out noise and improve the thermal resolution of both photon detectors and microbolometers.

2.2. Determining the thermal time constant experimentally using an optical chopper

As a first step in characterising microbolometer (MB) performance, it was decided to confirm the time constant value quoted by the manufacturer using the same setup that was presented in [11]. An Infrared Systems Development Corporation IR-2106/301 flat plate blackbody [19] was set to 30 °C and a Thorlab optical chopper (MC2000B-EC with MC1F2 blade [20]) at room temperature was placed between the microbolometer camera and the optical chopper as shown schematically in Fig. 1. The setup was enclosed using a blackout curtain to prevent any heat sources in the surrounding lab environment impinging on the chopper or blackbody. As the optical chopper rotates, its blade generates rectangular (square) waves with rotating frequencies of 4 to 40 Hz, i.e. those of interest for TSA. 100 images were captured at 25 and 50 Hz frame rates with the NR feature on and off. The chopper rotating frequency was changed from 4 to 40 Hz in 1 Hz intervals up to 11 Hz and then 2 Hz intervals up to 40 Hz. For the determination of the thermal time constant, only frequencies up to 11 Hz were considered as it was the maximum loading frequency considered in TSA experiments and below the Nyquist frequency for both frame rates.

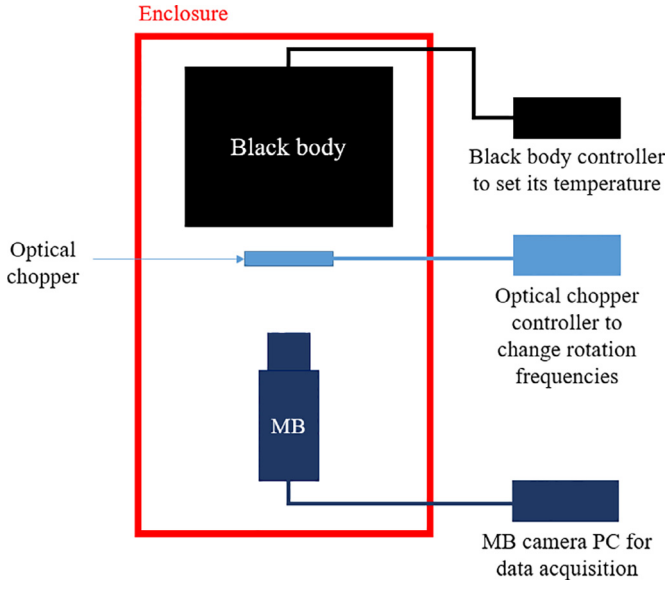

Fig. 1. Plan view of setup used to determine the thermal time constant of the microbolometer (MB).

Fig. 2 shows four images taken with the microbolometer with the blackbody in the background, and the optical chopper at room temperature in the foreground. Fig. 2 (a) and (b) show images with the NR feature on, while (c) and (d) show images with the NR off. As the NR on and off tests were not conducted together, the chopper temperatures are different by about 3 °C, which can be attributed to changes in the laboratory ambient conditions. The black symbols are single data points considered in the study (Fig. 2 (a), (c)) and four points marking a 10 x 10 pixel area shown in Fig. 2 (b), (d).

To check the accuracy of the rotation frequency setting of the chopper, the signal time series from a single pixel was processed into the frequency domain using a Fast Fourier Transform (FFT). Fig. 3 shows the frequency obtained with the FFT plotted against the optical chopper input frequency with the NR feature on at (a) 50 Hz and (b) 25 Hz frame rate. It can be seen in Fig. 3 (a) that from 4 Hz to 11 Hz, the optical chopper input frequencies do not match the values extracted with the FFT, probably because the optical chopper is designed to operate at larger rotational speeds. However, from 12 Hz up to 24 Hz the frequencies from the optical chopper input and FFT extraction match. It can be seen that the folding frequency is at 25 Hz, that is when the optical chopper frequency is half the frame rate (Nyquist frequency [21]). After 25 Hz, the FFT frequency reduces as the optical chopper rotation is undersampled. Similar behaviour can be seen in Fig. 3 (b). It is clear that the optical chopper cannot rotate as requested at the lower loading frequencies, hence, the frequencies considered to calculate the thermal time constant are those obtained from an FFT of the experimental data.

To obtain the parameters τ_{th} and C in Eq. (4), the Nelder-Mead Simplex algorithm [11] was used:

$$\min_{\{\tau_{th},\, C\}} \sum_i \left(\Delta T(\omega_i) - \frac{C}{\sqrt{1+\omega_i^2 \tau_{th}^2}} \right)^2 \tag{7}$$

where $\Delta T(\omega_i)$ is the magnitude obtained with the microbolometer, i.e. peak-to-peak temperature, ω_i is the chopper frequency in rad/s ($\omega = 2\pi f$ where f is frequency in Hz), and the subscript i corresponds to a particular rotating frequency.

Eq. (7) was solved using an iterative procedure within Matlab using the fminsearch function [22] to identify τ_{th} and C. Fig. 4 clearly shows that the fit of the experimental data to the model data obtained from Eq. (7) is closer to the NR off (Fig. 4 (d)). The offset in magnitude in Fig. 4 (a) and (b) compared with (c) and (d) is because there was a 3 °C variation of surface temperature of the optical chopper between the experiments with the NR on and those with it switched off. As mentioned above, the temperature difference is evident in the full field IR images shown in Fig. 2. It should be noted that the change in ambient temperature has little effect on the overall analysis as the basis for the assessment is a temperature change, rather than an absolute value. It is clear that the NR feature changes the response, hence the nature of this feature is explored in detail in the following section.

The thermal time constant obtained for each single point and region with and without NR applied in the microbolometer is presented in Table 2. It can be seen that in all cases the time constant obtained is smaller than 8 ms, which corresponds to the 'below 8 ms' as stated by the manufacturer [16]. It further is observed that the results obtained without the NR applied are more precise ranging from 5.2 ms to 5.9 ms, while the results with the NR activated varies from 4.3 ms to 7.2 ms, demonstrating that the NR feature strongly influences the response from transient signals. The exact nature of the NR feature is not described by the manufacturer, but it is clearly useful in reducing the noise for a stationary signal. However, in TSA the signal is transient and, hence, any averaging of the response will result in further filtering.

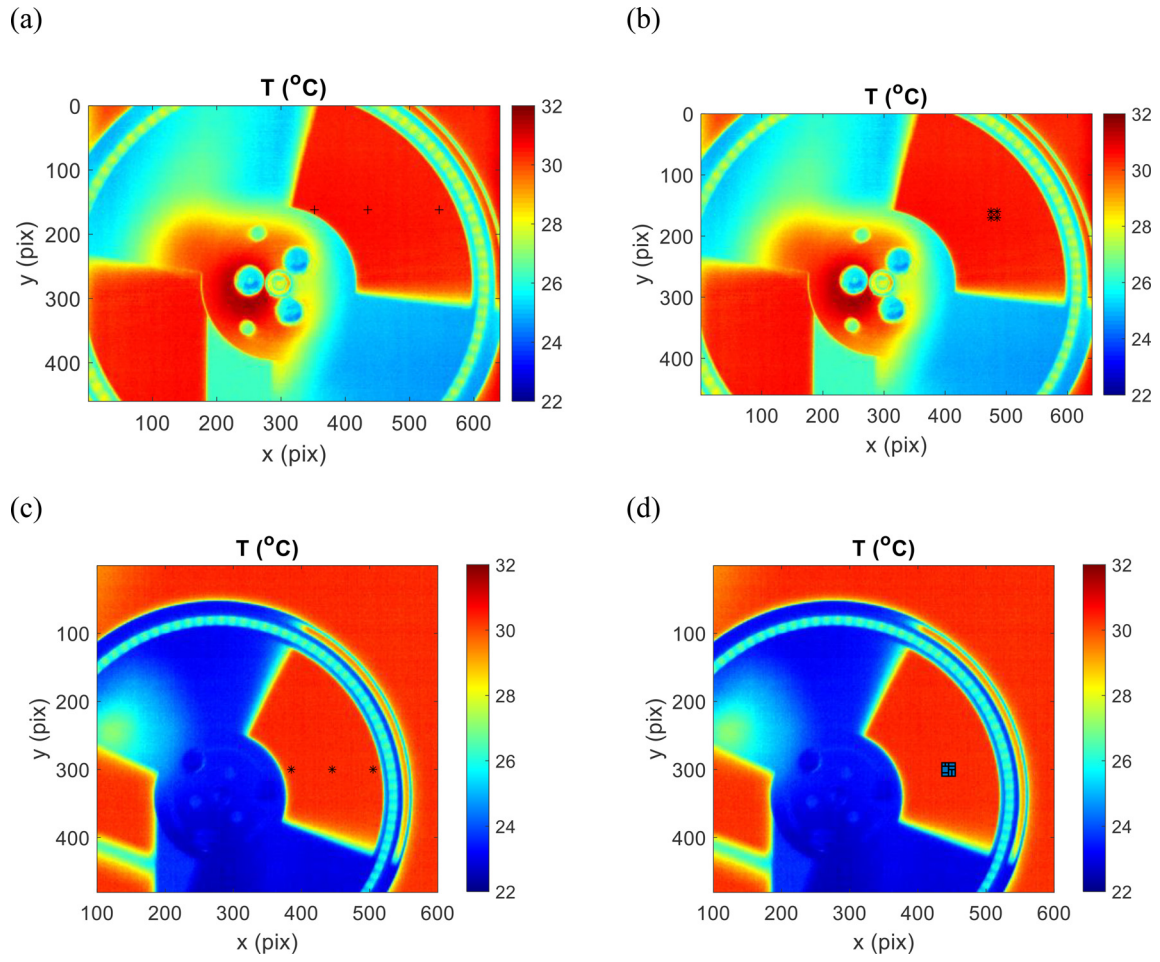

Fig. 2. Temperature (°C) field images of the optical chopper placed in front of the blackbody showing the (a) single pixel measurement points (NR on), (b) an averaged 10×10 pixel region (NR on), (c) single pixel measurement points (NR off) and, (d) an averaged 10 x 10 pixel region (NR off).

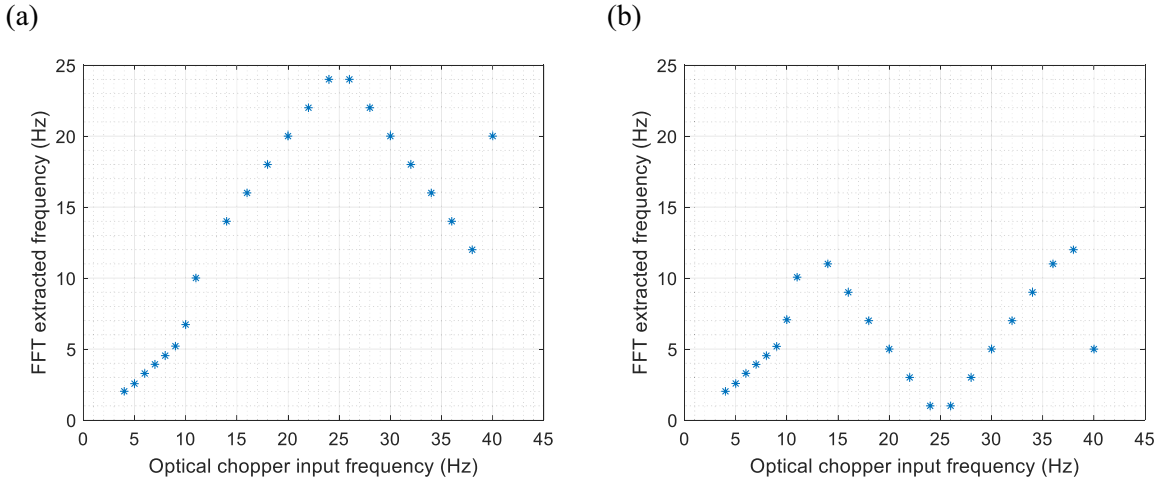

Fig. 3. Frequency obtained with FFT vs Optical Chopper Frequency with the microbolometer recording with NR applied at (a) 50 Hz frame rate and (b) 25 Hz frame rate.

2.3. Noise reduction simulation

To identify the nature of the NR feature, it is assumed that the NR feature performs a temporal averaging of the thermal data points to reduce the standard deviation in the readings. Therefore, the NR feature is represented as a rolling average in a simulated model with the magnitude of the NR scaled by varying the number of data points averaged (N) from 2 to 7. The simulation consists of creating a sinusoidal signal of a certain frequency (loading frequency (LF) for TSA experiments) and normalised amplitude sampled at 50 Hz, which is the maximum frame rate of the FLIR A655sc in full frame window mode. The signal is passed through a low-pass filter of 8 ms simulating the behaviour of the FLIR

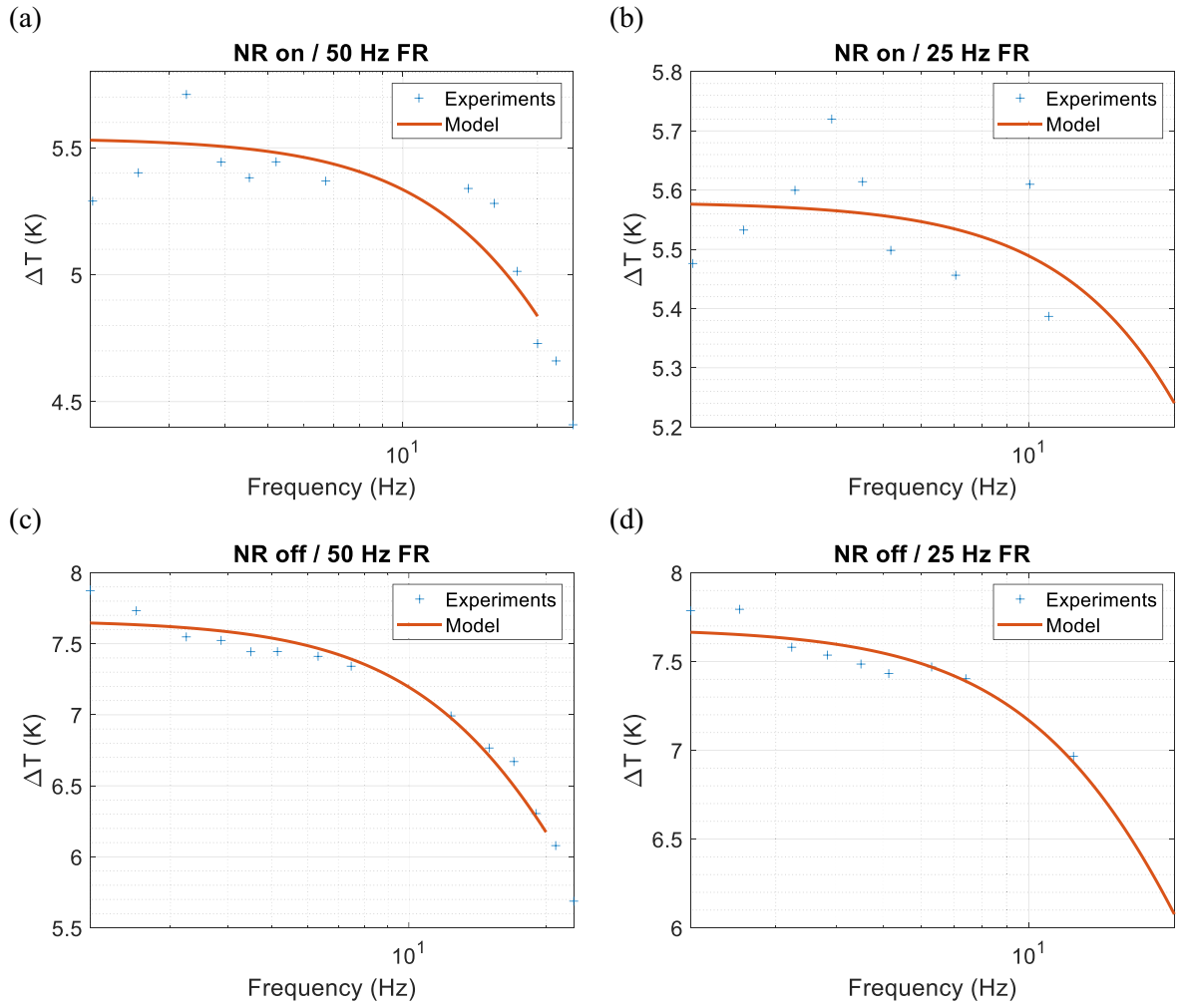

Fig. 4. Experiments fit to model (a) NR on and 50 Hz frame rate, (b) NR on and 25 Hz frame rate, (c) NR off and 50 Hz frame rate, and (d) NR off and 25 Hz frame rate.

Table 2
Thermal time constant obtained from optical chopper experiments at different single points and an averaged 10 x 10 pixel region with the microbolometer collecting data with the NR activated and deactivated.

NR		On		Off	
Frame Rate		50 Hz	25 Hz	50 Hz	25 Hz
Regions	Region	5.6 ms	5.2 ms	5.6 ms	5.2 ms
	Single outer pixel	4.3 ms	6.8 ms	5.5 ms	5.6 ms
	Single inner pixel	4.4 ms	6.9 ms	5.9 ms	6.2 ms
	Single central pixel	4.6 ms	7.2 ms	5.7 ms	5.9 ms

A655sc. A simple rolling average is applied to the output, which calculates the mean of the following N data points. Finally, a least-squares algorithm is used to extract the equivalent thermoelastic response (see Section 4). The simulation was carried out over a range of (loading) frequencies (ranging from 2.1 to 6.1 Hz) to obtain similar plots to those in Fig. 4, and to extract the time constant for each level of averaged points, N. An example of the process is illustrated in Fig. 5 for the case of a signal of 4.1 Hz loading frequency (LF) and $N = 6$ averaged points.

The normalised peak-to-peak amplitude with respect to the loading frequency is shown in Fig. 6 (a) for different N. It can be seen that the magnitude reduces when the frequency increases due to the low-pass filtering effect, and is further reduced when the number of average points increases. The time constant for each case of N is obtained using Eq. (7).

Fig. 6 (b) shows the time constant obtained with respect to N, where it can be seen that the increase of N produces a significant increase in the time constant, therefore, producing a low-pass filter effect far greater than the 8 ms time constant of the microbolometer. Hence, it can be concluded that the NR feature uses a rolling average of several data points and will result in additional attenuation of the response from a transient signal.

3. Test samples and experimental arrangements

Throughout the paper, different test samples are used to evaluate the performance of microbolometers for TSA; these are described in this section. Firstly, simple metallic strip test samples that can be loaded in uniaxial tension are used in Sections 4, 6 and 7 with dimensions given in Table 3. If K for the material is known, then the applied stress is determined directly so that Eq. (1) yields a predicted value of ΔT. This is compared with ΔT obtained from the microbolometer (see Section 6). Additionally, an Al 6081 T6 'Brazilian disc' [23] of 8 mm diameter and 6 mm thickness is used in Section 5 to show an example of temperature vs time signal.

To assess the possibility and implication of the application of microbolometer based TSA to fibre reinforced orthotropic polymer composites, unidirectional (UD) RP-528 [26] Glass Fibre Reinforced Polymer (GFRP) samples of 0 UD and 90 UD were used in Section 7. The dimensions of the GFRP samples are given in Table 4 and comprised 10

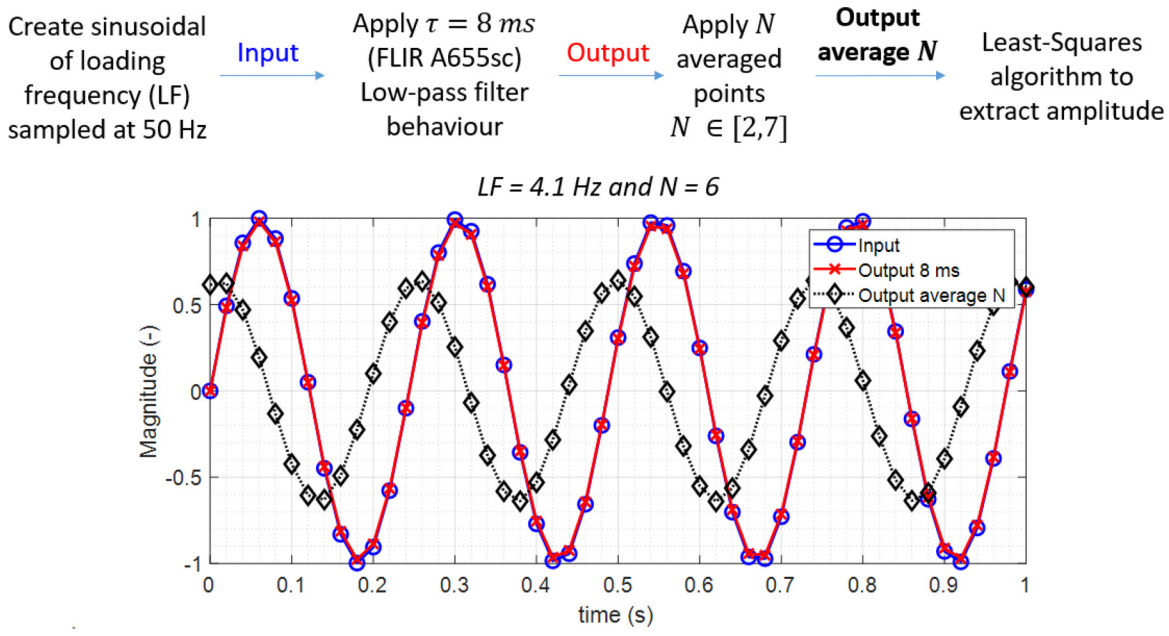

Fig. 5. NR simulation procedure for 4.1 Hz loading frequency and 6 averaged points.

Table 3
Metallic samples dimensions and thermoelastic constants.

Specimen	Gauge Length (mm)	Width (mm)	Thickness (mm)	K (MPa^{-1})
Al 6081 T6	50	15	6	$9.5 \cdot 10^{-6}$ [24]
316 L Stainless Steel	237	30	2	$4.6 \cdot 10^{-6}$ [25]

Table 4
RP-528 [26] GFRP UD sample dimensions.

Specimen	Length (mm)	Width (mm)	Thickness (mm)
0 UD: $[0]_{10}$	270	15	2.36
90 UD: $[90]_{10}$	235	25	2.36

plies, which were cured in an autoclave for 1 h at 120 °C and 4 bar. End tabs of the same material and were bonded to the UD specimens using an adhesive film.

To investigate the application of microbolometer-based TSA to CFRP composites, a specimen was manufactured from prepreg in a $[0, 90]_{6s}$ configuration to give a specimen that is 150 mm long, 35.81 mm wide and 5.16 mm thick. To simulate a subsurface manufacturing defect, the specimen was constructed as shown in Fig. 7 (a), which also shows a micrograph of the consolidated material and the effect of the ply drops, which form fibre waviness. The specimen was loaded in an Instron 8800 servo-hydraulic test machine to a stress level of 67.5 MPa so that a crack grew from the region of the ply drops. The extent of the delamination crack is shown in the X-ray CT-scan of Fig. 7 (b). The damaged CFRP specimen is used in Section 8.

For all the experiments described in the paper an Instron 8802 servo-hydraulic test machine was used to cyclically load the test samples. Each specimen was coated with a thin layer of Electrolube matt black paint (between 15 and 25 μm in all cases) to reduce reflections and create a surface with a uniform emissivity of 0.95 [27, 28] prior to mounting in the test machine.

Fig. 8 shows a plan view schematic of the test configuration. The microbolometer camera was positioned on one side of the machine so that the lens could focus on the sample and provide field of view that covered the region of interest. A blackout curtain was used as an enclosure to prevent any heat sources in the surrounding laboratory environment impinging on the test samples and being reflected into the camera. The curtain was mounted so that there was adequate ventilation to prevent the enclosure form heating during the tests. The computer used to acquire the images from the microbolometer camera was positioned outside the enclosure.

4. Influence of loading frequency on IR image processing

The thermoelastic response, ΔT, is extracted from a temperature time image series, $T(t)$, captured by the microbolometer. A least-squares fit to a sine wave with a loading frequency identical to that of the applied cyclic load is used to identify ΔT using the following expression:

$$T(t) = T_0 + \frac{\Delta T}{2} \sin(2\pi f t + \phi) \tag{8}$$

where T_0 is the mean temperature of the cycle and ϕ is the phase.

The least-squares fit is facilitated by rewriting Eq. (8) in terms of the in-quadrature amplitudes to remove the ϕ term:

$$T(t) = T_0 + C \cos 2\pi f t - D \sin 2\pi f t \tag{9}$$

where C and D are the unknown amplitudes.

The following matrix equation is solved for each pixel in the microbolometer detector array:

$$\begin{bmatrix} C \\ D \\ T_0 \end{bmatrix} = \begin{bmatrix} \cos 2\pi f t_1 & -\sin 2\pi f t_1 & 1 \\ \vdots & \vdots & \vdots \\ \cos 2\pi f t_n & -\sin 2\pi f t_n & 1 \end{bmatrix}^{-1} \begin{bmatrix} T(t_1) \\ \vdots \\ T(t_n) \end{bmatrix} \tag{10}$$

where n is the number of measurements, i.e. the total number of frames.

To give

$$T_0 = \frac{1}{n} \sum_{i=1}^{n} T(t_i) \tag{11}$$

$$\Delta T = 2\sqrt{C^2 + D^2} \tag{12}$$

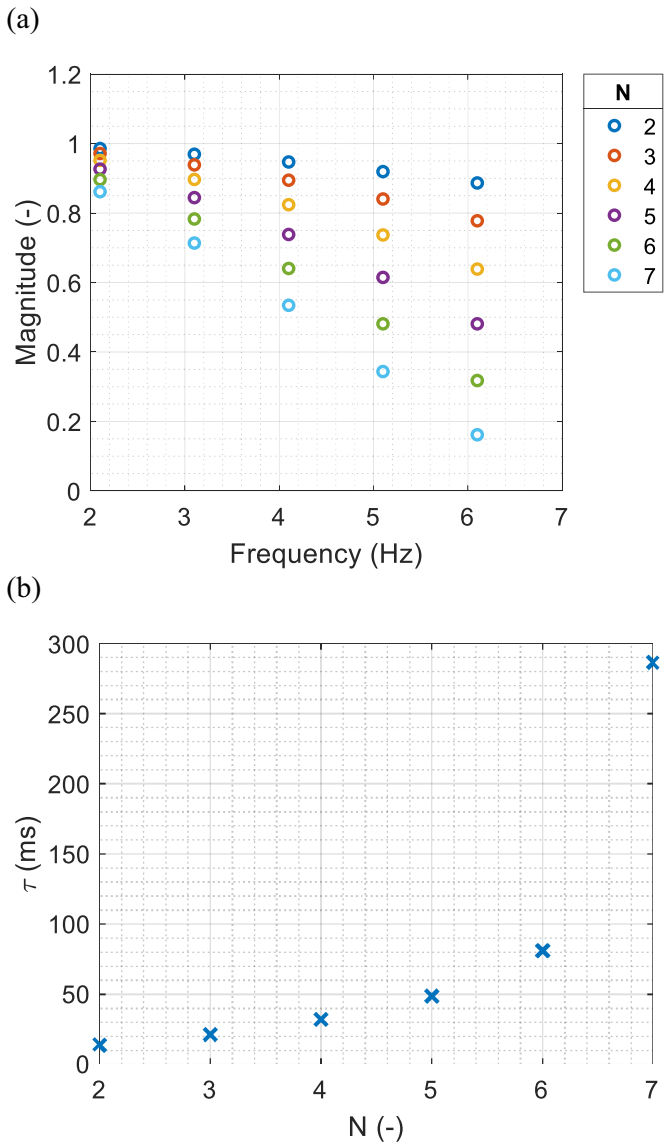

Fig. 6. (a) Magnitude vs frequency for each average number of data points, (b) time constant vs average number of data points.

$$\phi = \arctan \frac{D}{C} \tag{13}$$

The advantage with respect to the common lock-in algorithm is that the least-squares algorithm does not require an integer number of loading cycles and hence avoids any effects from spectral leakage. It should be noted, as with practically all microbolometer systems, that the FLIR A655sc does not have the capability to input an analogue signal from the test machine to time stamp the images, hence, a manual input of the frame rate and loading frequency is required. As the load is not synchronised with the image frames, phase data (Eq. (13)) cannot be considered.

As the least-squares fit results in an 'inverse notch' filtering of the temperature data, it is essential that the loading frequency at which the test was conducted is known accurately. The loading frequency is set on the test machine, but due to inertia and slackness in from test rigs and/or wear in the machine may not be generated on the test specimen exactly. It is possible to obtain the loading frequency by analysing the image series, but this may also introduce inaccuracies. Hence, the first step in the evaluation of the performance is to establish the effect of small variations in the loading frequency on the thermoelastic response.

In this section, the sensitivity of the loading frequency as a user entered input variable into the least-squares algorithm is studied. The experimental data is from the 316 L stainless steel coupon subjected to a cyclic load of 3 ± 1.79 kN at 6 Hz loading frequency. The loading amplitude was chosen to achieve a theoretical 80 mK ΔT response from the test specimen. The microbolometer camera was set to obtain images at a frame rate of 50 Hz and 25 Hz, with the NR feature switched on.

The least-squares algorithm processed the same dataset with loading frequencies entered into the software ranging from 5.8 to 6.2 Hz. Fig. 9 shows ΔT with respect to the loading frequency input into the software for experimental data collected at camera frame rates of 50 Hz (a) and 25 Hz (b). This illustrates that it is vitally important that the exact loading frequency is used, otherwise the thermoelastic response will be significantly attenuated. It is noteworthy that even at the exact 6 Hz loading frequency, the maximum ΔT peak is at 25 mK instead of 80 mK, as a consequence of the NR feature.

The notch filtering is essential for TSA as it allows the small change in temperature as a consequence of the applied stress, i.e. ΔT to be identified in a very noisy signal. When using photon detectors, it is possible to precisely obtain the loading frequency from the input of a reference signal into the camera by time stamping utilising the camera frame rate. With the microbolometer cameras it is typically the case that signals cannot be input, hence another means of identifying the loading frequency must be used. It is not recommended to simply input the desired loading frequency to the test machine because of potential inaccuracies in the control system. It has been clearly demonstrated that even if only a few percent away from the actual loading frequency, the signal is attenuated. A means of mitigation would be to use an FFT on the load signal from the test machine to check the loading frequency applied was the same as that requested in the test machine set-up. Additionally, the self-referencing approach as described in [29, 30] could be used to determine an exact loading frequency.

In TSA there is typically a low signal to noise ratio as the NETD for microbolometers is around 30 mK and ΔT can be much smaller than this. Furthermore, noise can be introduced by the surroundings, usually because of reflected radiation and motion of the specimen. Using the notch filtering as stated above allows the ΔT to be extracted from a noisy signal. However, determining the influence of noise on the ΔT value extracted from Eq. (8) using least squares fitting is informative.

A noisy signal was simulated in Matlab using a cyclic sinusoidal temperature signal of 293 K mean with peak-to-peak amplitudes varying from 0.02 K to 0.1 K combined with the noise signal. The noise signal comprised uniformly distributed random numbers centred at 0 with 30 mK amplitude. The simulation allows varying levels of input signal against a fixed level of noise at different frequencies ranging from 0.25 Hz to 11 Hz to be studied. It is important to note that the filtering effect of the time constant is not included in this part of the analysis to illustrate only the effect of the noisy signal in the image processing. The simulated data was sampled at 50 Hz (the maximum frame rate of a microbolometer) and processed using the least-squares algorithm to extract ΔT. Fig. 10 shows that the output from the least-squares algorithm corresponds to the input amplitude regardless of the frequency used. Therefore, the level of noise has no significant influence on the extraction of the thermoelastic response, ΔT, when the input is a noisy sinusoidal signal.

5. Microbolometer model to assess variations in waveforms

A Simulink model was developed as shown in the block diagram in Fig. 11 that enables known inputs to be processed using the least-squares algorithm to better understand how different input signals affect the output ΔT. The Simulink model consists of a low-pass filter, constructed as a block or RC circuit, with a thermal time constant of 8 ms as defined by the manufacturer of the FLIR A655sc. The input of the low-pass filter is a signal of 1 V amplitude with the same noise level as the NETD of the microbolometer (30 mK). The input signal can be any cyclic signal

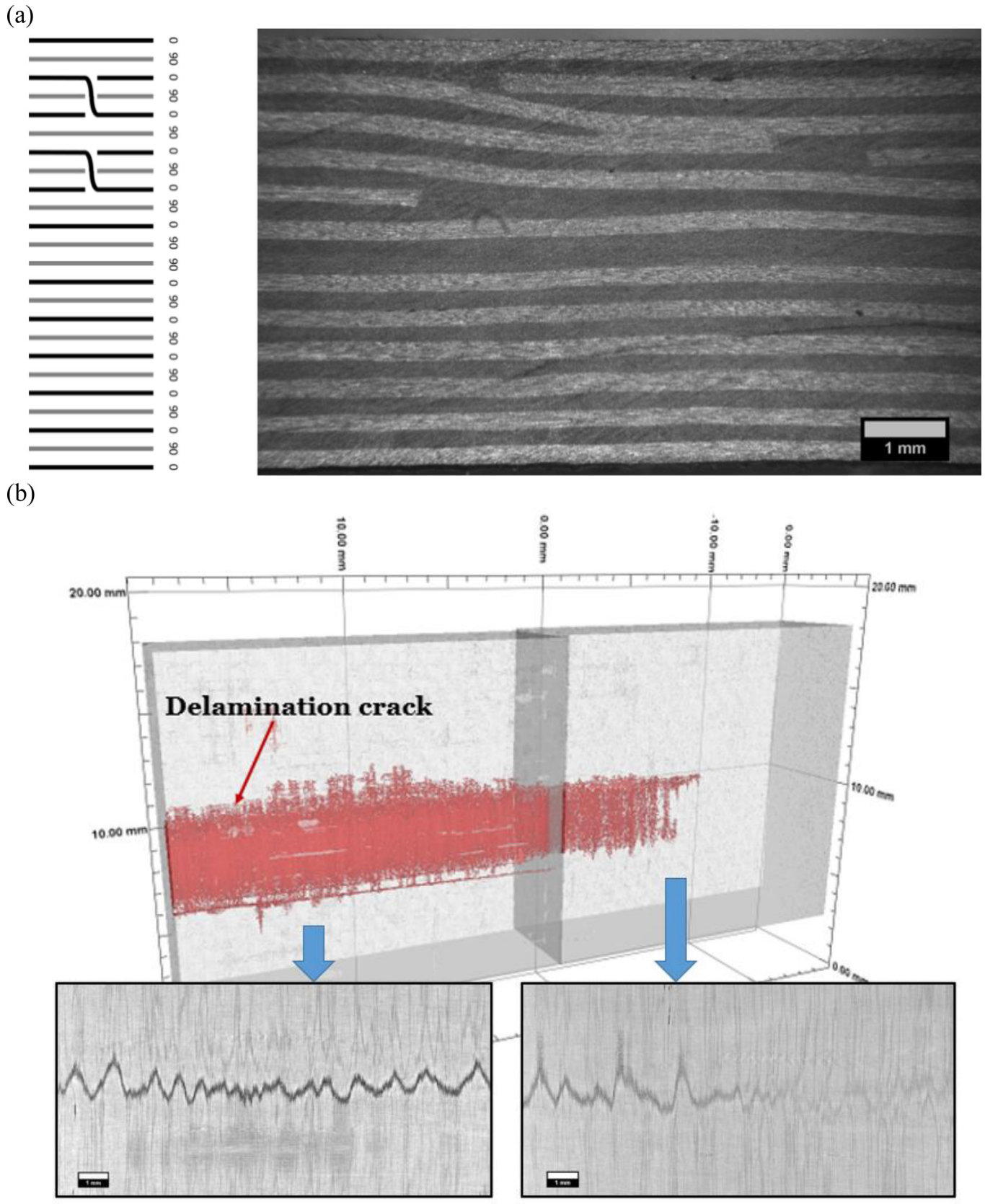

Fig. 7. (a) CFRP sample lay-up with embedded defect, thickness view, (b) 3D CT-scan of the developed delamination crack after 67.5 MPa stress level including main body of the cracked region and towards the edge of the cracked region.

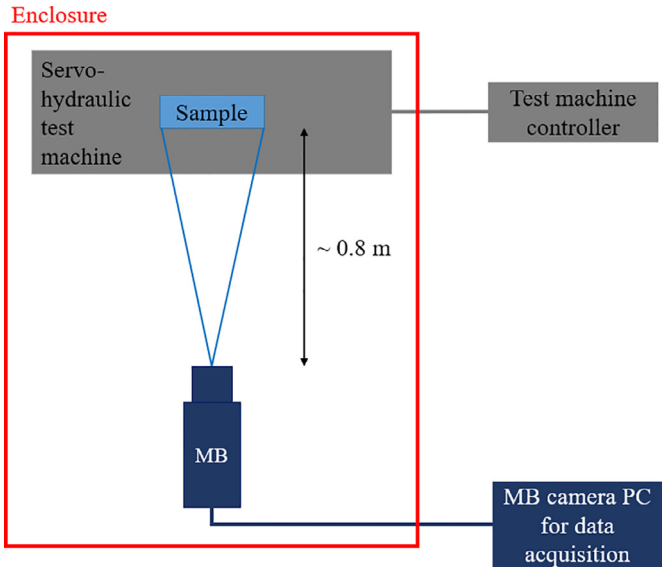

Fig. 8. TSA setup.

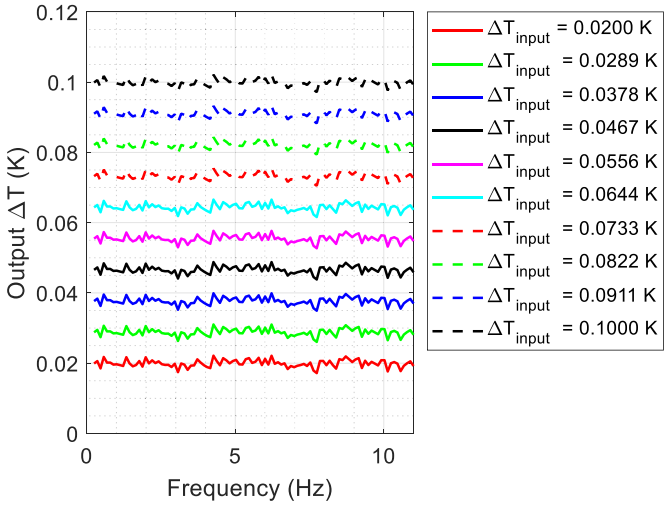

Fig. 10. Peak-to-peak amplitude vs loading frequency for different input signal magnitudes.

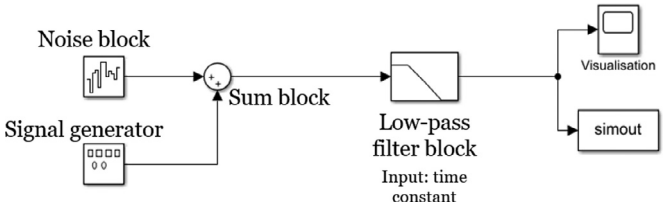

Fig. 11. Simulink model of a microbolometer based TSA measurement system.

(triangular, sawtooth, rectangular, sinusoidal, etc.) and a slope can be added to simulate mean signal drifting. The model outputs a visualisation window with the plot of the final signal (visualisation block) and a variable called 'simout' that allows discrete-time sampling of the output data. This output data is then imported into Matlab to be processed by the least-squares algorithm to calculate the change in voltage, ΔV, analogous to ΔT. The simout is sampled at 50 Hz matching the maximum frame rate of the camera. ΔV is normalised with the expected value, i.e. 2 V peak-to-peak.

To apply the least-squares fit to the thermal data, the assumption is that the input signal is sinusoidal, hence, variations in the input waveforms are studied, alongside changes in mean temperature, as the sample temperature and/or the sensor may drift during the test. TSA depends on the load amplitude, which in turn affects the signal to noise ratio, i.e. a greater stress results in a larger thermoelastic response. Hence, signals of different amplitudes are studied to give different signal to noise ratios. This will also simulate the effect of different materials and surface emissivities as these also affect the thermoelastic response. Under adiabatic conditions the thermoelastic response is independent of frequency, but it is clear from the description of the operating principles of a microbolometer that changing the loading frequency will have an effect on the derived thermoelastic response. Hence, a large range of different loading frequencies are used to investigate their effect on the thermoelastic response.

For microbolometer based TSA experiments, it is necessary to collect data over relatively long time periods to reduce noise. The downside to capturing data over long periods of time is the potential for the sample to increase temperature, hence drift of the mean temperature. It is therefore important to model the impact of temperature drift on the TSA output. Fig. 12 shows an example of the normalised temperature signal shifted to zero along time for a single pixel obtained from the aluminium Brazilian disc with the microbolometer FLIR A655sc, with the frame rate set to 50 Hz and the NR on. The temperature signal is obscured by noise,

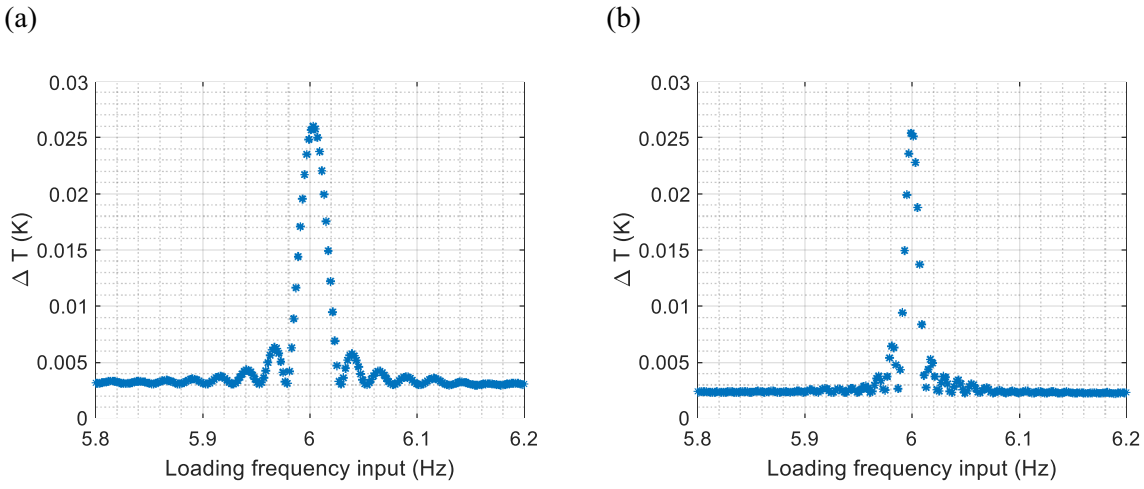

Fig. 9. ΔT vs loading frequency (LF) input on 316 L stainless steel at 6 Hz sampled at (a) 50 Hz frame rate and (b) 25 Hz frame rate.

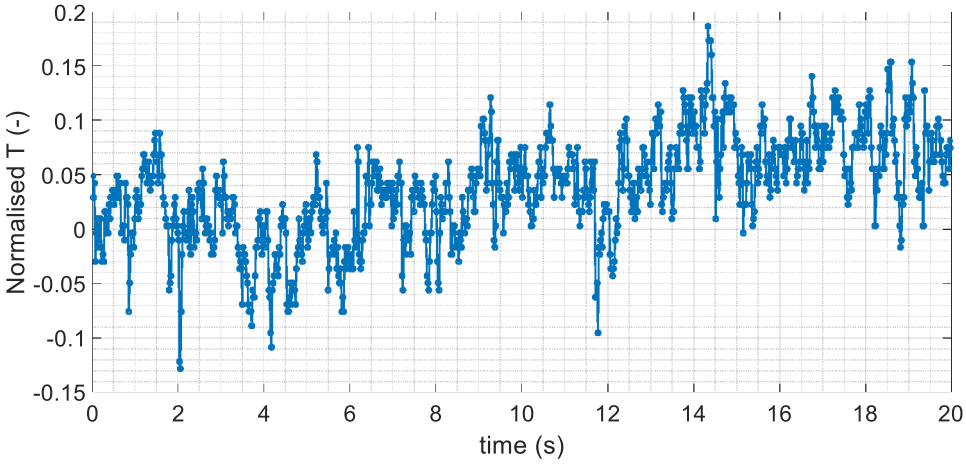

Fig. 12. Example of normalised temperature shifted to zero vs time of a single pixel during a sinusoidal test of a Brazilian disc loaded at -5 ± 2.25 kN at 2.1 Hz loading frequency.

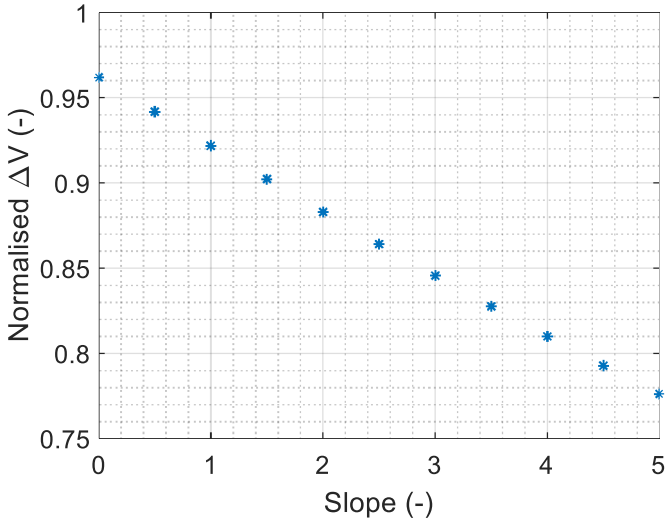

Fig. 13. Normalised output of 5 Hz frequency sinusoid vs slope added.

and it is evident that even over this relatively short time period, the microbolometer shows some drift in the mean temperature reading and that, although there is some evidence of periodicity, the temperature signal is not a sine wave. Hence, there is need to study the effect of the different input waveform shapes and signals with a drifting to the mean value on the final extracted value of ΔT.

To study the effect of drifting mean value, sine wave was used with different gradients on the mean level of slope from 0 to 5 V/s. Fig. 13 shows that increasing the slope attenuates the output ΔV. The data points of the curve presented in Fig. 13 can be fitted to the linear expression:

$$\Delta V = -0.0372 \cdot slope + 0.9591 \tag{14}$$

Therefore, the attenuation scales with the magnitude of the mean drift, but the gradients used here are extreme cases, as it would require unrealistic rapid increases in temperature not usually evidenced with the frequencies used for TSA.

Fig. 14 (a) and (b) show the normalised output (normalised ΔV), calculated as $\Delta V_{output}/\Delta V_{input}$, with respect to the loading frequency in (a) for a sawtooth with a harmonic at 10.1 Hz, and (b) the same signal as previously but with the addition of a 0.5 gradient slope. Application of Eq. (7) to the curves shown in Fig. 14 (a) and (b) gives time constant of 7.7 ms and 5.1 ms, respectively. As expected, the least-squares algorithm underestimates the output when a triangular waveform is used demonstrating that fitting to a sine waves requires a sinusoidal signal. With the addition of the mean drift, the output is further attenuated. It is clearly demonstrated that the quality of the sine wave is important for accurate TSA. In cases where it is not possible to apply a good quality sine wave, then a lock-in algorithm or FFT should be applied instead of a least squares fit to extract the parameters from Eq. (8).

6. Demonstration of the effect of experimental parameters on the thermoelastic response

Experiments were conducted on the stainless steel and aluminium alloy test specimens, described in Section 3 and Table 3. The servo-hydraulic test machine was used to apply a sinusoidal cyclic tensile load with 16 loading frequencies ranging from 0.25 to 40 Hz. For both test samples, ΔT was obtained using a pixel by pixel least squares fit (see Eq. (8)), 2000 images were captured by the microbolometer using four frame rates of 6.25 Hz, 12.5 Hz, 25 Hz and 50 Hz with the NR feature on and off. The applied loading amplitudes are given in Table 5. These were determined using Eq. (1) by assuming T_0 to be 293 K, so that ΔT values of approximately 50, 80 and 100 mK could be developed in the both sample materials. In total, 1320 tests (summarised in Table 6) were carried out, hence it was decided not to measure T_0 from the thermal image series using the least squares fit to Eq. (8), or by simply taking raw temperature measurement, as the load amplitude would require a small adjustment for each test. Instead, it was decided to accept a small error in the predicted value of ΔT and set load amplitudes to the those given in Table 5. In view of the many tests required to carry out the parametric study described above, the tests were not repeated. ΔT was extracted from data points over a large region of the surface of each sample hence repeat tests were not considered necessary as any non-uniformity or deviations would be apparent in the full field data.

The experimental values of ΔT ($\Delta T_{measured}$) were divided by the calculated value of ΔT (ΔT_{known}) given in Table 5 to give normalised values, i.e. $\Delta T_{measured}/\Delta T_{known}$, which in all cases should yield a values close to unity. Departures from unity indicate that the measured data is not following that prescribed by Eq. (1), so this treatment provides a means of investigating the efficacy of using microbolometers in TSA. It should be noted that a 5 K variation in specimen surface temperature away from the approximated 293 K to establish ΔT_{known} would result in around $\pm 1\%$ variation in $\Delta T_{measured}/\Delta T_{known}$ demonstrating that it is not necessary to obtain T_0 for each test.

In the interests of brevity, selected $\Delta T_{measured}/\Delta T_{known}$ values from the 1320 cases are plotted in Fig. 15 with respect to frame rate, load amplitude, material, loading frequency and NR feature on or off. Fig. 15 (a) shows $\Delta T_{measured}/\Delta T_{known}$ for the aluminium alloy specimen collected at a loading frequency of 1 Hz, with the NR off, against the frame rate for a loading frequency of 1 Hz. At higher loading frequencies (below the Nyquist frequency) and with the NR feature on the results were also con-

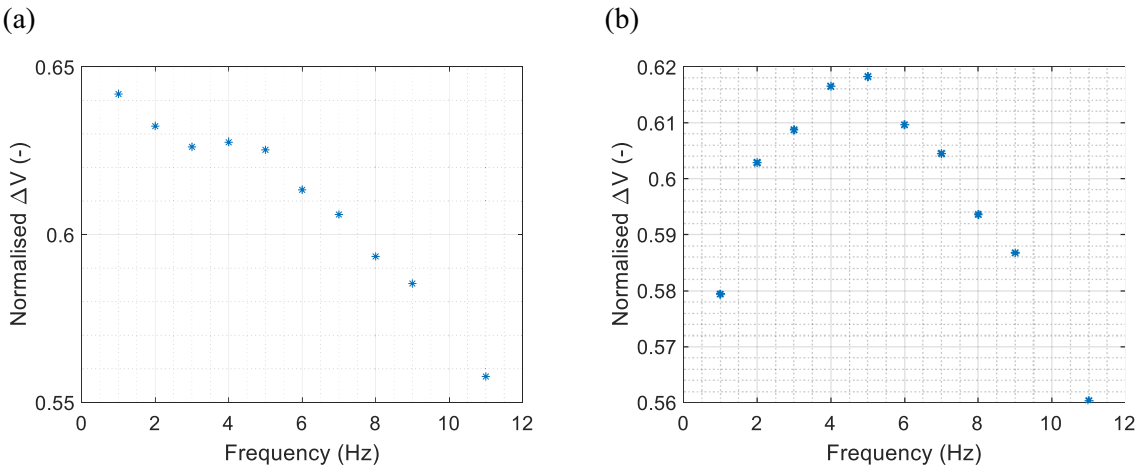

Fig. 14. Normalised output vs loading frequency of sawtooth signal with (a) an harmonic at 10.1 Hz and (b) an harmonic at 10.1 Hz and 0.5 gradient.

Table 5
Loading cases for the metallic specimens to achieve $\boldsymbol{\Delta T}$ values of 50, 80 and 100 mK.

Coupon	Loading case 1 (kN)	Loading case 2 (kN)	Loading case 3 (kN)
Al 6081 T6	2 ± 0.81	2 ± 1.30	2 ± 1.62
316 L Stainless Steel	3 ± 1.12	3 ± 1.79	3 ± 2.24
Predicted $\boldsymbol{\Delta T}$ (mK)	50	80	100

Table 6
Experiments performed.

Sample material	NR	Loading frequency (Hz)	Frame rate (Hz)	Load cases
Al 6081 T6	On	0.25, 0.5, 1, 2, 3, 4, 5, 6, 7, 8, 9, 10, 11	6.25, 12.5, 25, 50	1, 2, 3
	Off	1, 3, 5, 7, 9, 11, 13, 15, 17, 19, 21, 23, 26, 30, 35, 40	6.25, 12.5, 25, 50	1, 2, 3
316 L Stainless Steel	On	0.25, 0.5, 1, 2, 3, 4, 5, 6, 7, 8, 9, 10, 11	6.25, 12.5, 25, 50	1, 2, 3
	Off	1, 3, 5, 7, 9, 13, 17, 19, 21, 23, 26, 30, 35	6.25, 12.5, 25, 50	1, 2, 3

stant with frame rate but $\Delta T_{measured}/\Delta T_{known}$ was less than unity; similar results were obtained from the stainless steel specimen with the NR feature on. From this it is determined that at loading frequencies below the frame rate Nyquist frequency the frame rate has no effect on ΔT.

Fig. 15 (b) shows $\Delta T_{measured}/\Delta T_{known}$ from the aluminium alloy specimen for a loading frequency of 1 Hz and camera frame rate of 25 Hz with the NR off plotted against load amplitude; the results were constant for loading frequencies below the frame rate Nyquist frequency. Similar to the discussion on Fig. 15 (a), when the NR was turned on, and dependant on loading frequency, $\Delta T_{measured}/\Delta T_{known}$ decreased considerably in the same manner for both the aluminium alloy and stainless steel specimens, but remained constant for each load amplitude.

Fig. 15 (c) shows the effect of varying the loading frequency on $\Delta T_{measured}/\Delta T_{known}$ for both the aluminium alloy and stainless steel specimens for a frame rate of 25 Hz and load case 1, with NR off. There is a marked reduction in $\Delta T_{measured}/\Delta T_{known}$ for both materials, which is independent of the material. The result confirms that the microbolometer behaves as a low-pass filter.

Fig. 15 (d) shows a comparison of $\Delta T_{measured}/\Delta T_{known}$ against loading frequency, for a frame rate of 25 Hz and load case 1, with the NR on and off. It can be seen that with the NR on, there is a much greater attenuation in $\Delta T_{measured}/\Delta T_{known}$ than with NR off. As expected, the scatter in the data is much less with NR on compared to NR off. Fig. 15 (d) also shows the simulated data from the model in Section 5. For the NR on case the model required a time constant of 80 ms (solid red line), which is 10 times higher than the thermal time constant provided by the manufacturer, to match the experimental results. For the NR on the model required a 8 ms time constant (solid black line) to match the experiments.

In summary, the microbolometer performance only depends on the loading frequency, and greater attenuation is produced when the NR feature is turned on, i.e. corresponding to a higher time constant. It is concluded that if the NR feature is on, the response over a number of frames is averaged. The simulation carried out in Section 2.2 suggests that the NR feature may be averaging six frames, as this matches the time constant of 80 ms extracted from the experimental data. In [14], the same IR microbolometer camera was used for TSA, and the results obtained with the NR on, but the effect of the NR feature on the thermoelastic response output from the camera was not studied. Instead, the dependency on the loading frequency, i.e. low-pass filter behaviour, was accounted for by a stress 'calibration' of the thermoelastic response given in digital level (as described in [15]) at the loading frequency used for testing, with the NR feature enabled. However, it is clear from the work presented herein that the NR feature causes significant attenuation, especially when testing materials at high loading frequencies (> 10 Hz), which are considered necessary to achieve adiabatic behaviour. The work described in this section indicates that it is possible to define a unified calibration procedure for microbolometer based TSA that accounts for the attenuation, which is caused by the fixed time constant and the NR feature for a given microbolometer camera, to obviate the need to carry out the stress calibration [15] for each loading frequency used. Such a procedure is devised in the following section.

7. Calibration approach for microbolometer based TSA

To develop the calibration technique for microbolometer based TSA results from the aluminium and stainless steel samples presented in the previous section are used to develop the calibration procedure. Addi-

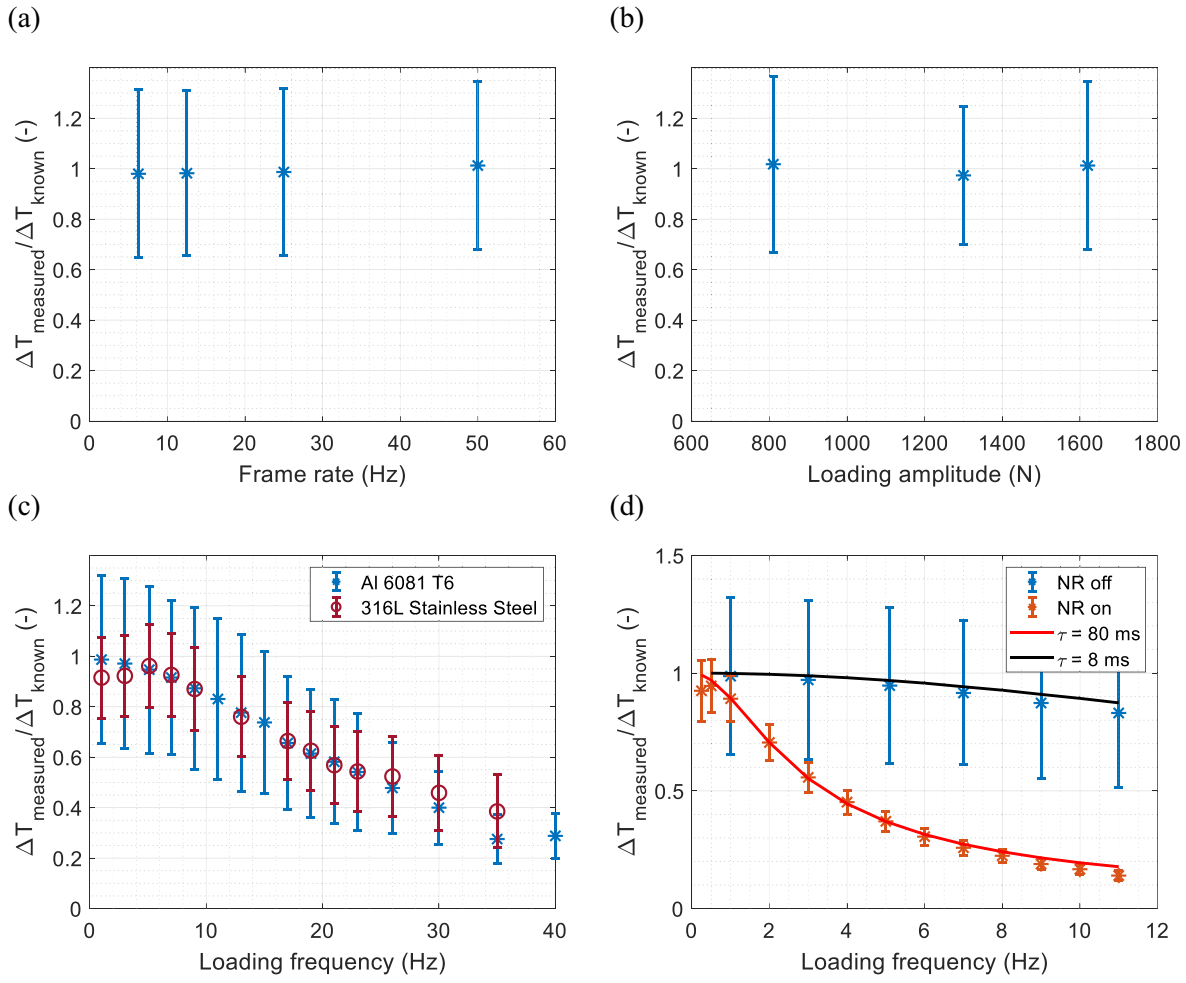

Fig. 15. Normalised thermoelastic response to study different factors affecting TSA: (a) frame rate (aluminium) NR off, (b) loading amplitude (aluminium) NR off, (c) loading frequency and material with NR off and (d) NR comparison (aluminium).

Table 7
Loading cases for the GFRP specimens.

Coupon		Loading case 1	Loading case 2	Loading case 3
0 UD GFRP $[0]_{10}$	**Load (kN)**	2 ± 1.84	3 ± 2.94	4 ± 3.68
	ΔT_{known} measured with the photon detector (mK)	68	115	141
90 UD GFRP $[90]_{10}$	**Load (kN)**	1 ± 0.43	1 ± 0.69	1 ± 0.87
	ΔT_{known} measured with the photon detector (mK)	52	84	105

tionally, GFRP composite materials (described in Section 3) were included in the study to investigate any effect of material anisotropy. In contrast with the metallic samples, the GFRP specimens were tested without applying paint as the epoxy resin has a high emissivity [31]. As the value of the response from the GFRP specimen is a function of the stress and the coefficient of thermal expansion [32], a photon detector (FLIR SC5500) was used to obtain the ΔT_{known} value, and this was subsequently used to provide $\Delta T_{measured}/\Delta T_{known}$. The photon detector viewed one side of the specimen whilst the microbolometer viewed the other side. Data acquisition for both the photon detector camera and the microbolometer were started at the same time for the GFRP specimens. Both IR detectors collected 2000 frames for each measurement, however, due to the differences in frame rate of the IR cameras, the microbolometer captured data over a much longer time period compared with the photon detector. The applied loads for the experiments on the GFRP are given in Table 7 alongside the ΔT_{known} obtained from the photon detector.

$\Delta T_{measured}/\Delta T_{known}$ is plotted against loading frequency over the range 0.25 to 11 Hz, for all four material types in Fig. 16. Fig. 16 (a) presents the results with the NR feature on, and includes values taken at the three different load cases for each material with a camera frame rate of 50 Hz. It is clear that the only variable that has a significant effect on $\Delta T_{measured}/\Delta T_{known}$ is the loading frequency. There is generally an excellent agreement with the model, although there is considerable scatter in the data at very low loading frequencies, which could be attributed to heat transfer effects, but are well below the loading frequencies typically used for TSA. Fig. 16 (b) shows the results for the NR off, for the metallic specimens only and only one load case for the stainless steel. There is significant variation for each load case resulting in a poor fit to the model at the higher loading frequencies. The variation with NR off is clearly evidenced in Fig. 15 indicating that despite the large number of images captured, for most TSA studies it would be necessary to have the NR feature on. It is important to note that the cut-off frequency, calculated using Eq. (6), is 1.99 Hz when the NR is on (τ_{th} = 80 ms),

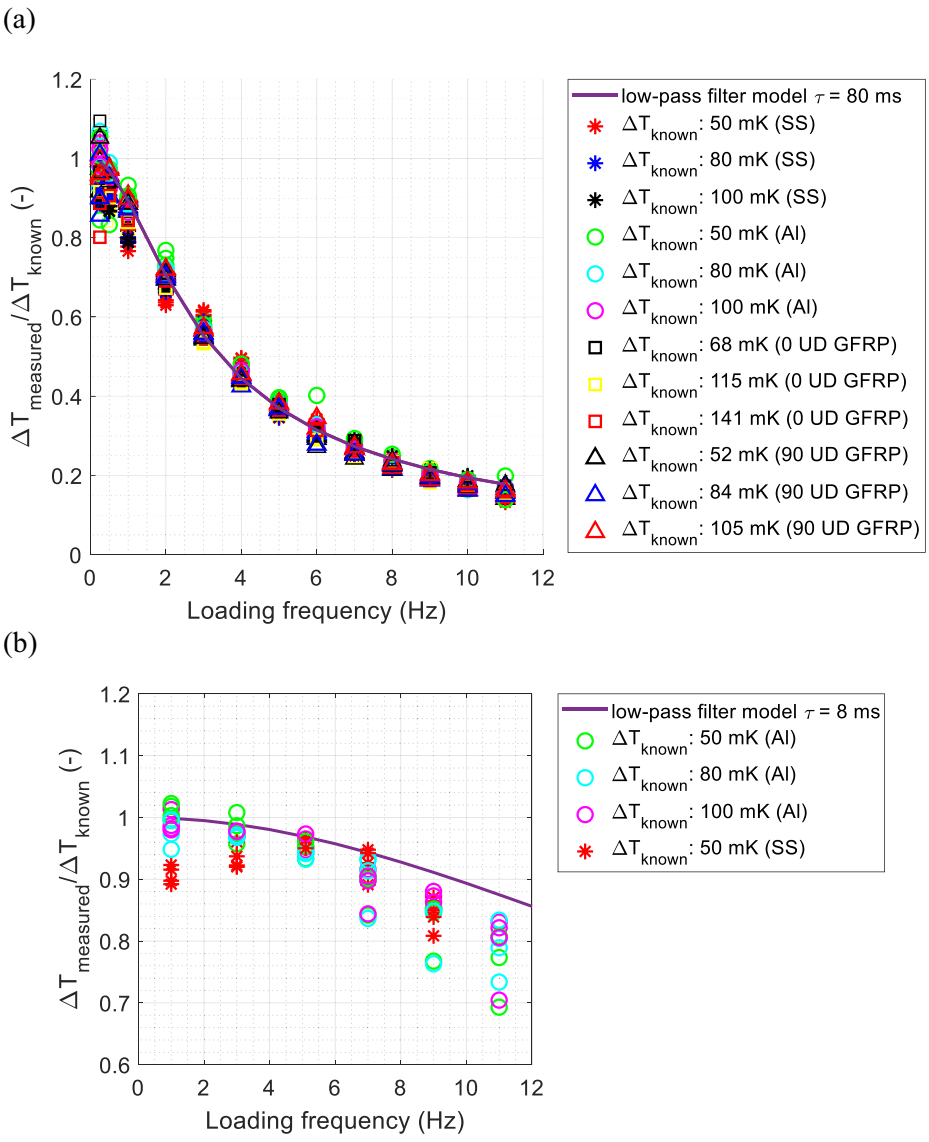

Fig. 16. Simulink and experimental data comparison (a) NR on and (b) NR off.

but 19.89 Hz when NR is not applied ($\tau_{th} = 8$ ms). The very low cut off frequency with NR on means that for most situations the measured thermoelastic response will be less than the actual value, meaning the derived stress will be non-conservative, hence a means of calibrating that accounts for the filtering effect is essential. The next step is to devise a simple calibration procedure that does not require that a known value of τ_{th} to be deduced. As the use of NR feature considerably reduces the noise in the thermoelastic response (see Fig. 15 (d)) and the filtering is most severe, the remainder of the paper concentrates on analysis with the NR on.

The data presented in Fig. 16 (a), can be linearized by presenting it as a gain Bode diagram as shown in Fig. 17 with a common logarithmic scale, where it can be seen that the attenuated thermoelastic response follows a linear trend for loading frequencies greater than the cut-off frequency of 2 Hz.

Fig. 17 clearly confirms that the attenuation is independent of material and load, and depends exclusively on the loading frequency. Based on this finding, a suitable calibration technique that corrects for the dependency on loading frequency can be devised. The proposed approach simply requires a coupon specimen with a known thermoelastic constant, such as 316 L stainless steel. The coupon is loaded in tension, with an applied stress that produces a known ΔT, and thermal image series are collected with the NR on and off over a range of loading frequencies. Hence, a calibration parameter, CP, is defined as follows:

$$CP = \frac{\Delta T_{known}}{\Delta T_{measured}} \tag{15}$$

where ΔT_{known} is the calculated temperature change for the applied stress, and $\Delta T_{measured}$ is the measured temperature change obtained from the microbolometer thermal image series using the image processing algorithm.

Fig. 18 shows the linearised presentation of the data shown in Fig. 17 as follows:

$$20 \log CP = A \cdot f_0 + B \tag{16}$$

where f_0 is the loading frequency, A is the slope and B is the intercept.

The CP can be extracted from Eq. (16) as follows:

$$CP = 10^{\left(\frac{Af_0+B}{20}\right)} \tag{17}$$

so that it can be used to calibrate other materials when using TSA with the microbolometer system and NR feature considered for a particular f_0.

The parameters A and B are established with the NR feature on as 1.512 Hz^{-1} and 0.363, respectively, from a linear fit of the data in Fig. 18.

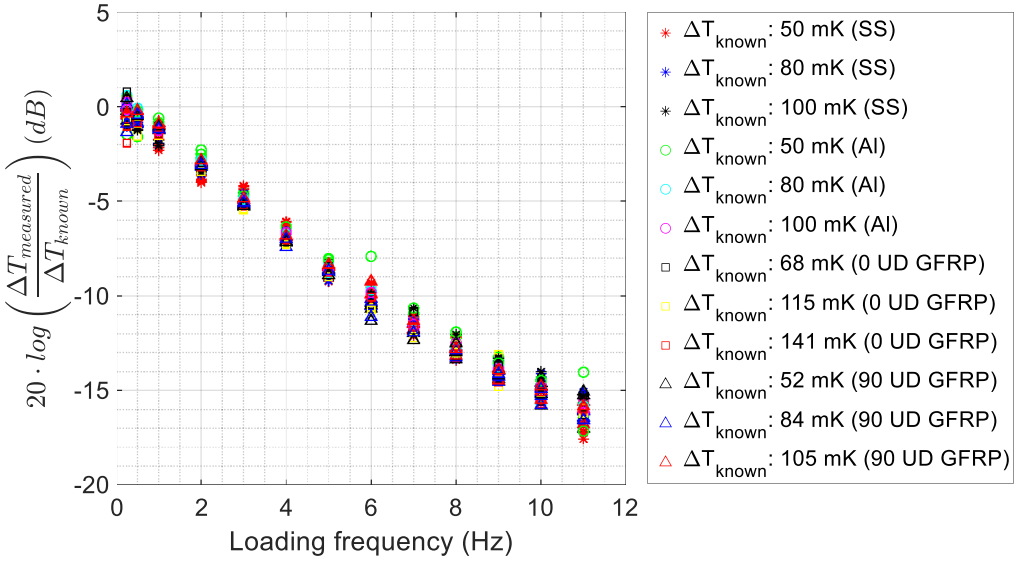

Fig. 17. Normalised measured temperature change vs loading frequency with the NR on.

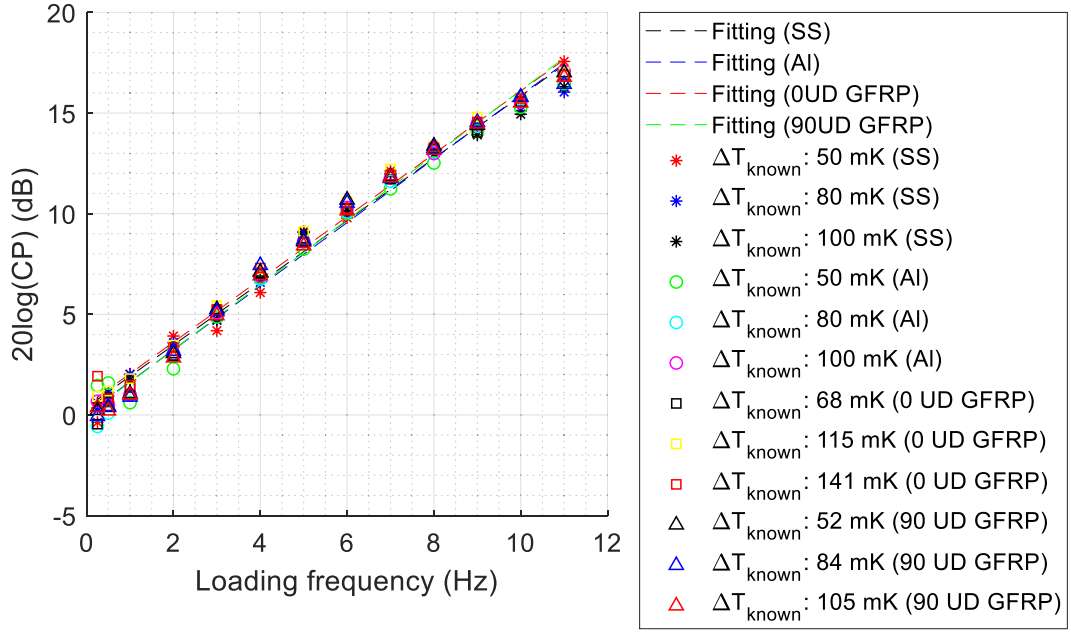

Fig. 18. Calibration fitting for stainless steel (SS), aluminium (Al), and 0 UD and 90 UD GFRP specimens (NR on).

For the general case, the effect of any inbuilt NR feature is unknown, and hence, an experimental validation is essential. It should be noted that with the NR feature off, as the time constant of the microbolometer is known, the CP can be obtained analytically from the normalisation and inverse of Eq. (4) as follows:

$$CP = \sqrt{1 + \left(2\pi f_0\right)^2 \tau_{th}^2} \tag{18}$$

The above has demonstrated how a CP can be obtained for TSA with microbolometers. The calibration is performed after ΔT has been obtained by the image processing, and simply involves multiplying the measured ΔT by the calibration parameter, CP. Hence, previous knowledge of the structure in terms of geometry or material is not required as suggested in [13]. The calibration technique presented here is also different to that suggested by Rajic and Rowlands in [11], where the calibration was performed before the processing of the thermal data series and had to be applied to all the image frames, which requires more processing time than the calibration approach presented here.

8. Application of the calibration parameter

It was demonstrated that the calibration technique does not depend on the sample material, specimen temperature or magnitude of response, but only on the loading frequency and the NR feature. Therefore, it can be used to calibrate the thermoelastic response derived from the microbolometer image series on a range of materials, and on systems exhibiting variations of thermoelastic response, e.g. in the presence of a crack or stress gradients. Hence, to validate the use of the calibration parameter, a demonstrator in the form of a damaged CFRP specimen was used, as described in Section 3. The specimen was loaded at 25 kN mean and 20 kN amplitude at 5 Hz loading frequency.

The TSA results for the CFRP sample are presented in Fig. 19, where the ΔT is shown in Fig. 19 (a) for the uncalibrated microbolometer, in Fig. 19 (b) for the calibrated microbolometer and in Fig. 19 (c) for the photon detector. Bicubic image interpolation was applied to downsample the microbolometer IR data to have the same dimensional reso-

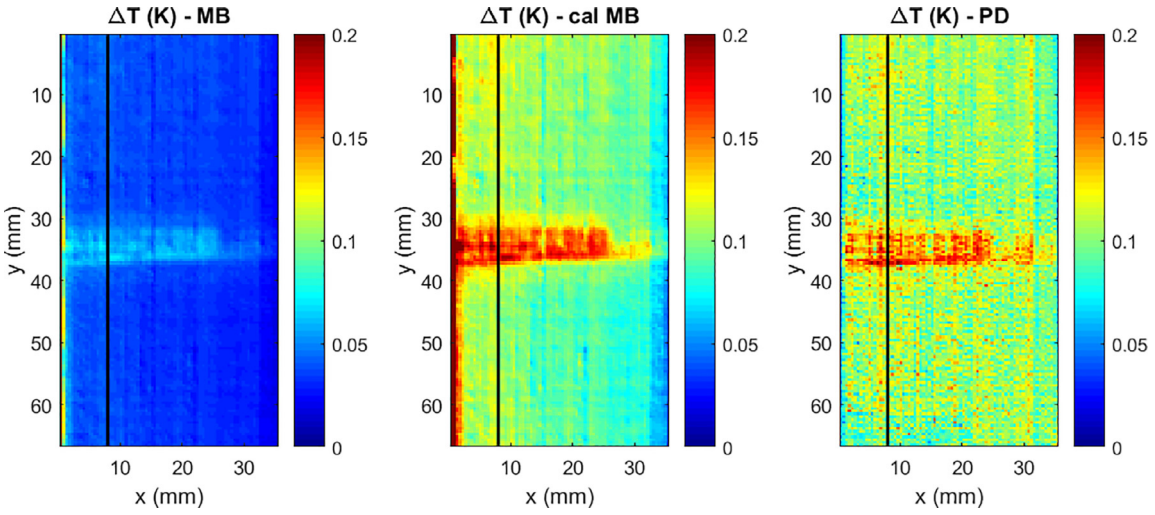

Fig. 19. ΔT results obtained in a CFRP specimen with (a) uncalibrated (uncal) microbolometer (MB), (b) calibrated (cal) microbolometer (MB) and (c) photon detector (PD).

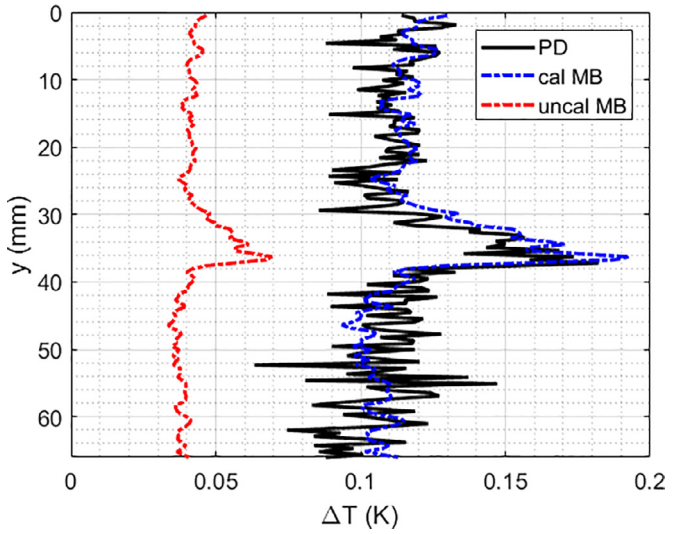

Fig. 20. Temperature change of the CFRP specimen obtained with TSA along the vertical length at 8 mm from the left edge with the photon detector (PD) and the calibrated (cal) and uncalibrated (uncal) microbolometer (MB).

lution as the photon detector, which is 0.46 mm/pix, to enable quantitatively comparison of the thermoelastic response of the sample captured with both IR detectors. The microbolometer was calibrated by scaling the magnitude of ΔT by 2.78, which corresponds to the CP at 5 Hz loading frequency (NR on). It is shown that the full-field temperature change maps from the photon detector and the calibrated microbolometer are nearly identical in terms of ΔT magnitude. Fig. 19 indicates that the area affected by subsurface crack is around 4 to 7 mm on the vertical scale of the mages. This is corroborated by the CT-scan in Fig. 7 (b), which shows that the width of the crack is approximately 5 mm. The similarity between the photon detector and calibrated microbolometer is further confirmed by comparing a line profile (x = 8 mm), corresponding to the black vertical line shown in Fig. 19, across the surface shown in Fig. 20. It can be seen that there is more noise present in the photon detector data in comparison with the microbolometer data. The lower noise can be attributed to more frames collected with the microbolometer (8000 frames) versus the photon detector camera (1000 frames). The microbolometer ΔT fields present edge effects due to the motion that affects all the data. The photon detector data was motion compensated by applying pencil markers on the surface and tracking the movement with the Altair software [33]; general motion compensation is being developed and will be presented elsewhere.

9. Conclusions

An analytical procedure based on Matlab Simulink was devised to assess how various features in the thermal image series affect the application of microbolometers to TSA. It was seen that for test with load amplitudes that vary over time, such as cyclic loading, and, particularly, at higher loading frequencies, the microbolometer behaves as a low-pass filter, which has an effect on attenuating the output magnitude and shifting the phase of the recorded temperature. The low-pass filter behaviour is driven by an inherent fixed time constant of the microbolometer sensor material, associated with the physical principles of how it converts IR radiation to an electrical signal.

It was shown that in-built NR feature further attenuates the thermal data from a transient scene and effectively increases the time constant which has a significant effect on the ΔT derived from the thermal image series. Using an optical chopper, the thermal time constant with NR off was determined as 'below 8 ms', which matched with the value provided by the manufacturer. However, with the NR on, the time constant measured did not match the value specified by the manufacturer as accurately as with the NR off. To model the NR feature, a rolling average approach was used, allowing the level of NR to be adjusted by changing the number of averaged data points in the signal. The model tested different numbers of averaged points (to change the level of NR) across different loading frequencies to test the attenuation on the TSA data. The study showed an increase of the time constant leading to an exponential attenuation when the number of averaged data points increased. Different TSA experiments were carried out to assess the effect of the camera frame rate, loading frequency, NR feature and material. It was shown the low-pass filter behaviour of the microbolometer and the increase of 10 times the time constant occurred only when the NR feature was activated. However, the camera frame rate, material, and loading amplitude did not have any influence on the measured ΔT with the microbolometer.

Due to the lack of an analogue input port in the camera to directly input the load signal from the test machine and time stamp with the camera frame rate, the loading frequency must be inputted manually into the least-squares algorithm. It is shown that as the algorithm behaves as a notch filter, it is essential that the loading frequency is determined

accurately. This can be done by various means e.g. using the infra-red image series or by an FFT or the image time series.

Different types of input signal were evaluated and showed that the least-squares algorithm overpredicts rectangular and sea-wave signal shapes, but underpredicts triangular signals. It is therefore important that a sinusoidal waveform is used with the least-squares algorithm. For signals such as rectangular and triangular, other algorithms such as lock-in are better suited.

The most important outcome from the work is the development of a calibration parameter that accounts for the attenuation of the thermoelastic response as loading frequency increases. The calibration parameter can be calculated directly using the microbolometer time constant provided by the manufacturer when NR features are disabled. However, when NR is used, it must be derived experimentally. The calibration approach obviates the need to calibrate at given frequencies or using a frame by frame approach as the approach is applied to processed TSA data. The calibration approach was applied and validated on a CFRP test specimen with an embedded crack. The experiments were performed with a photon detector and a microbolometer with the NR feature on. The comparison of ΔT between the calibrated microbolometer, and photon detector at the same spatial resolution matched closely.

Declaration of Competing Interest

The authors declare that they have no known competing financial interests or personal relationships that could have appeared to influence the work reported in this paper.

Data Availability

Data will be made available on request.

Acknowledgements

This work was supported by the Engineering and Physical Sciences Research Council [grant number EP/P006701/1], as part of the EPSRC Future Composites Manufacturing Research Hub. The work forms the basis of techniques developed for the Structures 2025 facility constructed using an EPSRC Strategic Equipment Grant (EP/R008787/1). The experimental work described in the paper was conducted in the Testing and Structures Research Laboratory (TSRL) at the University of Southampton. The authors acknowledge the support received from Dr Andy Robinson, the TSRL Principal Experimental Officer.

References

[1] Dulieu-Barton JM. Thermoelastic stress analysis. Optical methods for solid mechanics. Rastogi P, Hack E, editors, Weinheim: Wiley-VCH; 2012. ch. 8.
[2] Alshaya A, Shual X, Rowlands R. Thermoelastic stress analysis of a finite orthotropic composite containing an elliptical hole. Exp Mech 2016;56(8):1373–84. doi:10.1007/s11340-016-0174-x.
[3] Dulieu-Barton JM, Battams GP. Thermoelastic stress analysis and digital image correlation to assess composites. In: Society for experimental mechanics, 7. New York LLC: Springer; 2017. p. 283–6. doi:10.1007/978-3-319-41766-0_34.
[4] Potter RT. Stress analysis in laminated fibre composites by thermoelastic emission. Proc SPIE - Int Soc Optic Eng 1987;731:110–21. doi:10.1117/12.937892.
[5] Patterson E, Pitarresi G. A review of the general theory of thermoelastic stress analysis. J Strain Anal Eng Des 2003;38(5):405–17. doi:10.1243/2F03093240360713469.
[6] Rajic N, Wong AK, Lam YC. A thermomechanical technique for measuring residual stress. Exp Tech 1996;20(2):25–7. doi:10.1111/j.1747-1567.1996.tb01493.x.
[7] Budzier H, Gerlach G. Thermal infrared sensors: theory, optimisation and practice, Chichester: Wiley; 2011. [Online]. Available: https://ebookcentral.proquest.com/lib/soton-ebooks/reader.action?docID=699437™query .
[8] DISTEK Measuring Instruments. "FLIR SC5200 SC5500 SC5600 SC5650 high sensitivity and accuracy infrared Camera for industrial/educational therography." http://www.distek.ro/en/Product/Flir-SC5200-SC5500-SC5600-SC5650-High-Sensitivity-and-Accuracy-Infrared-Camera-for-Industrial-Educational-Therography–2063 (accessed 2017).
[9] Rajic N, Street N. A performance comparison between cooled and uncooled infrared detectors for thermoelastic stress analysis. Quant Infrared Thermogr J 2014;11(2):207–21. doi:10.1080/17686733.2014.962835.
[10] Wong AK, Rajic N, Nguyen Q. 50th anniversary article: seeing stresses through the thermoelastic lens-A retrospective and prospective from an Australian viewpoint. Strain 2015;51(1):1–15. doi:10.1111/str.12116.
[11] Rajic N, Rowlands D. Thermoelastic stress analysis with a compact low-cost microbolometer system. Quant Infrared Thermogr J 2013;10(2):135–58. doi:10.1080/17686733.2013.800688.
[12] Budzier H, Karause V, Böhmer S, Gerlach G, Hoffmann U. Fast microbolometer-based infrared camera system. presented at the 9th International Conference on Infrared Sensors & Systems Nürnberg , Germany; 2006. [Online]. Available: http://www.dias-infrared.de/pdf/p020.pdf .
[13] Vieira RB, Gonzáles GLG, Freire JLF. Thermography applied to the study of fatigue crack propagation in polycarbonate. Exp Mech 2018;58(2):269–82. doi:10.1007/s11340-017-0341-8.
[14] Pitarresi G, Cappello R, Catalanotti G. Quantitative thermoelastic stress analysis by means of low-cost setups. Opt Lasers Eng 2020;134. doi:10.1016/j.optlaseng.2020.106158.
[15] Dulieu-Smith JM. Alternative calibration techniques for quantitative thermoelastic stress analysis. Strain 1995;31(1):9–16. doi:10.1111/j.1475-1305.1995.tb00949.x.
[16] FLIR. "FLIR A655sc infrared camera." http://www.flir.com/science/display/?id=46802 (accessed 2018).
[17] Agarwal A, Lang JH. *First-Order transient in lineal electrical networks* (foundations of analog and digital electronic circuits). San Francisco: Morgan Kaufmann; 2005.
[18] Peeters J, Louarroudi E, De Greef D, Vanlanduit S, Dirckx JJJ, Steenackers G. Time calibration of thermal rolling shutter infrared cameras. Infrared Phys Technol 2017;80. http://dx.doi.org/10.1016/j.infrared.2016.12.001.
[19] Infrared Systems Development Corporation. IR-2106/301 blackbody system [Online] Available: https://www.infraredsystems.com/Products/blackbody2106.html
[20] Thorlabs Inc. "MC2000B." https://www.thorlabs.com/thorproduct.cfm?partnumber=MC2000B (accessed 2020).
[21] Fruehmann RK, Dulieu-Barton JM, Quinn S, Tyler JP. The use of a lock-in amplifier to apply digital image correlation to cyclically loaded components. Opt Lasers Eng 2015;68:149–59. doi:10.1016/j.optlaseng.2014.12.021.
[22] The MathWorks Inc. "fminsearch." https://uk.mathworks.com/help/matlab/ref/fminsearch.html (accessed 2020).
[23] Timoshenko S, Goodier JN. Theory of elasticity. 3rd Ed. McGraw Hill Asia; 2010.
[24] MakeItFrom. "Material Properties Database." https://www.makeitfrom.com/material-properties/6081-6081-T6-AlSi0.9MgMn-Aluminum (accessed 2018).
[25] United performance metals. "316 and 316L stainless steel sheet, coil & bar - AMS 5524, 5507, UNS S31600, S31603." https://www.upmet.com/products/stainless-steel/316316l (accessed 2018).
[26] *Toughened Epoxy Prepreg System RP-528*, Dorset, England, UK, 2016.
[27] Robinson AF, Dulieu-Barton JM, Quinn S, Burguete RL. Paint coating characterization for thermoelastic stress analysis of metallic materials. Meas Sci Technol 2010;21(8):085502. doi:10.1088/0957-0233/21/8/085502.
[28] Howell GP. Identification of plastic strain using thermoelastic stress analysis. Doctor of philosophy, engineering materials. University of Southampton; 2017.
[29] Tighe RC, Howell GP, Tyler JP, Lormor S, Dulieu-Barton JM. Stress based nondestructive evaluation using thermographic approaches: from laboratory trials to on-site assessment. NDT and E Int 2016;84:76–88. doi:10.1016/j.ndteint.2016.08.005.
[30] Sakagami T, Izumi Y, Mori N, Kubo S. Development of self-reference lock-in thermography and its application to remote nondestructive inspection of fatigue cracks in steel bridges. Quant Infrared Thermogr J 2010;7(1):73–84. doi:10.3166/qirt.7.73-84.
[31] Emery TR, Dulieu-Barton JM, Earl JS, Cunningham PR. A generalised approach to the calibration of orthotropic materials for thermoelastic stress analysis. Compos Sci Technol 2008;68:743–52. doi:10.1016/j.compscitech.2007.09.002.
[32] Jiménez-Fortunato I, Bull DJ, Thomsen OT, Dulieu-Barton JM. On the source of the thermoelastic response from orthotropic fibre reinforced composite laminates. Composites, Part A 2021;149. doi:10.1016/j.compositesa.2021.106515.
[33] FLIR Systems Inc. "FLIR instrument customer support center." https://support.flir.com/SwDownload/app/RssSWDownload.aspx?ID=171 (accessed.